Crystal structure and spectroscopic determination of the phase transitions in methylammonium- and formamidinium bismuth iodide perovskites

M. Bukleski[a,*], S. Dimitrovska-Lazova[a], V. Makrievski[a], P. Tzvetkov[b], M. Marinšek[c], T. Skalar[c], D. Kovacheva[b], S. Aleksovska[a]

[a]University "Ss Cyril and Methodius", Faculty of Natural Sciences and Mathematics, Institute of Chemistry, Arhimedova 5, 1000 Skopje, N. Macedonia

[b]Institute of General and Inorganic Chemistry, Bulgarian Academy of Sciences, Acad. G. Bonchev Str, Bd.11, 1113 Sofia, Bulgaria

[c]University of Ljubljana, Faculty of Chemistry and Chemical Technology, Večna pot 113 1000 Ljubljana, Slovenia

[*]corresponding author e-mail: mihabukleski@pmf.ukim.mk

Abstract

Understanding of the structural properties of hybrid organic-inorganic perovskites (HOIPs) and their behavior is crucial for their use as photovoltaics and for the design and assembly of solar cells. As part of this work, a detailed study was conducted to further understand bismuth iodide perovskites, with a specific focus on the phase transitions of methylammonium and formamidinium analogs. A detailed analysis of the temperature-dependent IR spectra was also performed in order to analyze the structural changes that occur. The presence of five phases in the methylammonium bismuth iodide (MABiI) and four phases in formamidinium bismuth iodide (FABiI) were determined. An additional confirmation of the reported results was obtained from the differential scanning calorimetry. The ambiguities concerning the crystal structure of FABiI were resolved based on the results by X-ray powder diffraction (XRPD).

Keywords: methylammonium bismuth iodide, formamidinium bismuth iodide, perovskite, phase transition, IR spectroscopy, XRPD

1. Introduction

Hybrid organic-inorganic perovskites (HOIPs) are most likely to be the materials of the future. They exhibit unique properties that have a wide variety of applications. One example is using HOIPS in solar cells due to their exceptional light-harvesting properties. The increasing need for clean energy has driven the search and synthesis of new perovskite compounds. The first study regarding the application of the organic-inorganic perovskites ($CH_3NH_3PbI_3$ and $CH_3NH_3PbBr_3$)

as materials for photovoltaic purposes was carried out by Kojima *et al*. that increases the solar cells with efficiencies of up to 3.8 % [1]. A few years later, a breakthrough was made by Kim *et al.* using mixed HOIPs as hole-transporting material to fabricate mesoscopic solid-state solar cells leading to the prevention of the decomposition of perovskite in the polar electrolyte solvent with device efficiency exceeding 9 % [2]. In the last decade alone, intensive research on perovskite solar cells led to an increase in efficiency of up to 31.3 % [3].

The effectiveness of the organic-inorganic perovskites, above all, is related to metal-halogen bonds (B–X) that are part of the octahedral coordination polyhedra as their main structural motif. In the perovskite structure (designated with general formula ABX_3) the octahedra are forming cubooctahedral cavities in which the A-cation is located [4], leading to an ideal cubic structure. In the organic-inorganic perovskites, the A position is usually occupied by a small organic cation, the B site is in the octahedra center and is occupied by a metal cation, and X is the inorganic anion, usually some halogen element. Many combinations of cations and anions can be used while retaining the perovskite structure. This leads to the possibility of modeling the composition of the perovskites and tuning their properties. Most of the recently studied HOIPs have methylammonium (MA) and formamidinium (FA) cations in the A position, even though other cations such as guanidinium [5], hydroxylammonium [6], hydrazinium [7], imidazolium [8], pyrrolidinium [9], azetidinium [10], etc. have also been used to synthesize these hybrid materials. In all of these combinations, the typical corner-sharing perovskite motive is kept, but different kinds of deviations from the ideal cubic structure appear leading to lower symmetry [11] and/or lower dimensionality. Today are known perovskites that belong to different crystal classes as well as with 3, 2, 1, or 0 dimensionality [12].

As mentioned, the first breakthrough in using HOIPs as light harvesting materials was achieved by utilizing organic lead iodides. Knowing the impact of lead on the environment and its potential toxicity (even though PbI_2, one of the products of the decomposition of lead HOIPs, is water insoluble and has low bioavailability), other HOIPs have been synthesized and used in solar cell development [13]. Therefore, one of the challenges was to replace the Pb^{2+} ion in the B position of the perovskites with a more suitable metal ion that would be environmentally friendly but would maintain an appropriately low bandgap. One of the most promising new emerging candidates to replace lead in the lead-iodide perovskites was tin ($CH_3NH_3SnI_3$). Despite the more difficult synthesis, it was determined that the power conversion efficiency of the solar cells made out of Sn instead of Pb have more or less similar values [14]. Soon after, the toxicity of Sn compared to Pb was questioned and it was found that the Sn-containing compounds have similar toxicity as the Pb-based systems. Since the synthesis of Sn-based HOPIs is more time-consuming and demanding, they have been abandoned and attention has been directed towards less toxic elements such as bismuth [15] and antimony [16]. Recently, several studies concerning the methylammonium and formamidinium bismuth analogs have been published [17–20]. It was shown that by using bismuth, not only has the toxicity been reduced, but the stability of the

HOIPs has also increased. Namely, MA and FA bismuth iodides are more stable towards atmospheric water and oxygen than their lead counterparts. Unfortunately, most of the Bi-based systems underperform when used in solar cells compared to the corresponding Pb and Sn analogs. A new possibility for bismuth HOIPs rose when combined with Pb and Sn analogs. A recent study by Yamada at all. [21] has shown that this kind of combination can yield higher power conversion. Another approach to improve the desired properties is by substituting part of the organic cation with another organic or even inorganic cation. In this way, double A-site mixed perovskites were obtained [22]. The organic and inorganic cations occupying the A site in the perovskite structure can also improve the conversion factor.

The possibilities offered by bismuth containing HOIPs directed our investigation toward $(CH_3NH_3)_3Bi_2I_9$ (MABiI) and formamidinium bismuth iodide, $[(CH(NH_2)_2]_3Bi_2I_9$ (FABiI). In this study, the structural characteristics and phase transitions in the mentioned compounds were analyzed aiming toward a better understanding of their stability.

The single crystal structure of MABiI was determined for the first time in 1990 by Jakubas *et al*. [23] and it was found to adopt a hexagonal $P6_3/mmc$ space group, being isomorphous to $Cs_3Sb_2I_9$, at room temperature. More than 25 years later, the crystal structure was reported again by several other authors, independently. The results are based on single crystal [24–26], thin films [22,27–29], and powder obtained by ball milling [17]. Only in two cases, structural refinements led to a different space group. Ajjouri *et al*. [17] have been working on a sample obtained by ball milling and found a space group $C12/c1$ that belongs to the monoclinic crystal system. The same crystal system was determined in the work of Hoye *et al*. [27]. Hoye *et al*. have been working on thin films on glass and quartz substrates, while in the rest of the studies, [22,28,29], MABiI has been deposited on TiO_2 substrates. An interesting fact arising from the analysis of the literature data for MABiI is that the space group found by Hoye *et al* is the same as the one found for the low-temperature phase (–113 ºC) in the work of Kamminga *et al*. [25].

Unlike MABiI, the interest in FABiI began to develop recently. The first report on its crystal structure based on single crystal XRD analysis was in 2019 by Szklarz *et al*. [19], even though two years earlier Shin *et al*. [28] prepared films on SnO_2 and TiO_2 substrates. The crystal system found by Szklarz *et al*. was hexagonal and the space group $P6_3mc$. Structural analysis of the compound prepared by ball milling led to space group $C12/c1$ (similarly to MABiI) [17]. In 2021, Li *et al*. [20] solved the structure of FABiI in the $P6_3mc$ space group.

In the current work, the crystal structures of powder MABiI and FABiI perovskites are analyzed, and some ambiguities present in the literature concerning the room temperature phase, have been resolved. One of the drawbacks of the perovskites used for solar cell production is the phase transitions (PT) they exhibit in the range of the operational temperature. That is why a detailed thermal analysis using differential scanning calorimetry (DSC) starting from –160 up to +200 ºC

has been conducted in order to characterize the phase transitions that take place. Valuable insight into structural changes was obtained by IR studies in a wide temperature range. The spectroscopic techniques were shown to be a valuable tool in the determination of the new phases. Based on the results of the IR analysis, more detailed attention was directed toward the results obtained by the DSC. In addition to the already mentioned techniques, the obtained samples were analyzed by scanning electron microscopy (SEM) imaging, energy dispersive X-ray (EDX) spectroscopy, and CHN analysis.

2. Experimental

2.1. Synthesis

Formamidinium iodide $CH(NH_2)_2I$, denoted as FAI, and **methylammonium iodide**, CH_3NH_3I denoted as MAI were used as starting materials in the synthesis of the bismuth iodide perovskites. For the synthesis of FAI, a stoichiometric ratio of formamidinium acetate (99 %, Alfa Aesar) and concentrated HI (57 % *w*/*w*, aqueous solution, stabilized with 1,5 % H_3PO_2, Carlo Erba reagents) were used. Under constant stirring, the acid was slowly added to the acetate. The obtained product was recrystallized from ethanol. MAI was synthesized by dropwise addition of HI to methylamine solution (40 % *w*/*w*, aqueous solution, Sigma - Aldrich) until reaching a pH of 8 – 8.5 while keeping the temperature at around 0 °C. The excess water and unreacted methylamine were removed by evaporation and the crude iodide was recrystallized from methanol.

Bismuth(III) iodide, BiI_3 was also pre-synthesized. It was obtained by dissolving Bi_2O_3 (99.9 %, Sigma-Aldrich) in concentrated HI. The obtained BiI_3 was recrystallized from an ethanol solution.

The synthesis of **formamidinium bismuth iodide**, $[(CH(NH_2)_2]_3Bi_2I_9$, was carried out in a 50 mL glass flask with temperature-controlled heating in an oil bath and constant stirring. For obtaining the product, pre-synthesized FAI (in 10 % excess) and BiI_3, were dissolved in 57 % HI. The solution was then heated to 120 °C. The reaction was allowed to proceed for 2 h 30 min and afterwards, the mixture was cooled down to room temperature. During cooling, crystallization of the perovskite occurred and the crystals were removed from the bottom of the flask, washed three times with dry ether, and placed on a watch glass. The crystals were dried for 1 hour at 100 °C in a vacuum dryer. After drying, they were stored in a desiccator.

The synthesis of **methylammonium bismuth iodide**, $(CH_3NH_3)_3Bi_2I_9$, proceeds identically to the synthesis of FABiI. For the synthesis of 1 g of the product, pre-synthesized 0.317 g of MAI (10 % excess) and 0.712 g of BiI_3 were used. As with the previous synthesis, it is important to carefully monitor the temperature because it must not exceed 130 °C.

2.2. Thermal analysis

The thermogravimetric and differential thermal analyses (TG/DTA) were carried out on Netzsch STA 449 F3 Jupiter apparatus. The measurements were performed in three steps. Heating from 35 to 800 ºC with a heating rate of 2 ºC min^{-1}, thermostating at final temperature for 1 h, and cooling down to 35°C with a cooling rate of 2 ºC min^{-1}. All segments were performed using an argon 5.0 atmosphere with a 50 mL min^{-1} flow rate and an Al_2O_3 crucible as reference material.

The DSC measurements were performed on a Mettler Toledo TGA/SDTA 851 instrument from –160 to 220 ºC. A heating rate of 5 ºC min^{-1} was used for dynamic measurement. The furnace was purged with air atmosphere at 100 mL min^{-1} flow rate. The samples were placed in 40 μL Al standard crucibles.

2.3. X-ray powder diffraction

X-ray powder diffraction (XRPD) patterns of the samples were collected at room temperature in an air atmosphere. The powder patterns were recorded using a Bruker D8 Advance powder diffractometer with CuKα radiation and a high-speed LynxEye PSD detector within the 2θ range starting from 6 up to 90 ° with 0.7 °/min scanning speed and 0.02 °2θ step size. The crystal structure refinements were performed using the Rietveld method and FullProf Suite (version July 2017) software package [30]. FullProf program allows the use of linear combinations of spherical harmonics to model anisotropic crystallite size line-broadening effects. This type of correction was necessary to model the powder pattern profile of methylammonium bismuth iodide, $[(CH_3NH_3)]_3Bi_2I_9$. The microstructural size model Size-Model=19 (Laue classes 6/*m* and 6/*mmm*) was used, as described in the FullProf manual. The powder pattern of sample formamidinium bismuth iodide, $[(CH(NH_2)_2]_3Bi_2I_9$ showed no signs of anisotropic line broadening, hence microstructural models were not applied during the crystal structure refinement. The interatomic distances, angles, bond-valence sums, and octahedral distortion for all samples were calculated using the Bond_Str (version July 2010) program, also part of FullProf Suite.

2.4. Scanning electron microscopy and EDX

The morphology and elemental composition of the samples were studied by field-emission scanning electron microscopy FE-SEM Zeiss Ultra Plus microscope. The samples were fixed using double-sided graphite tape onto the aluminium stub. The sputtering was not performed before microscopy. Images were taken using In-lens and/or standard Evernhart-Thornley secondary electrons (SE) detectors.

Infrared spectroscopy

The IR absorption spectra were recorded on a Perkin-Elmer System 2000 FTIR Spectrometer using Liquid Nitrogen Cell (LNC). For the absorption measurements, the KBr pellet technique

was used. The absorption spectra were recorded with a resolution of 2 cm^{-1}, using 32 scans (both for the background and the sample spectra) in the temperature range starting from –170 ºC up to 200 ºC and again down to room temperature on the same pellet. The CO_2/H_2O software compensation was used to reduce the intensity of the bands originating from the atmospheric moisture and the CO_2 outside the temperature-controlled cell. The IR spectra were recorded with a five-degree interval between each temperature allowing for a detailed analysis of the temperature-dependent changes that occur. Additionally, a one-degree temperature difference was set in order to record the temperature in the vicinity of the phase transition.

3. Results and Discussion

The elemental compositions of the phases were analyzed using EDX and CHN analysis. The results of the combined elemental analyses are shown in Table 1. Based on the obtained values, it can be concluded that the composition of these two perovskites is close to the expected one, having the stoichiometry of $A_3B_2X_9$, i.e. $A_3Bi_2I_9$.

Table 1. Theoretically calculated and experimentally obtained values for the elemental composition of the MABiI and FABiI.

	Element/ (*w*/%)	C	H	N	Bi	I
MABiI	theoretical	2.18	1.10	2.54	25.23	68.96
	CHN analysis	2.10	1.51	3.09		
	EDX				24.97	69.06
FABiI	theoretical	2.13	0.89	5.96	24.65	67.37
	CHN analysis	2.08	1.20	7.13		
	EDX				24.31	67.30

The SEM micrographs of the obtained perovskites are given in Figs. 1 and 2. The micrographs reveal hexagonal bifrustum-shaped crystals. It appears that FABiI forms more regularly shaped hexagonal bifrustum crystals with congruent top and bottom hexagons, while MABiI is rather less regularly shaped. The maximal size of crystals is ~100-150 μm and up to ~500 μm for MABiI and FABiI, respectively (Fig. 1a and 2a). Furthermore, the images showed that the obtained FABiI consists of well-formed crystallites compared to MABiI meaning that during the final stages of product synthesis FABiI crystals are somewhat easier to obtain than MABiI. The MABiI or FABiI crystals on their surface retain some remains from the mother solution as well as some adsorbed smaller crystals of the same phase (Fig. 1b and 2b).

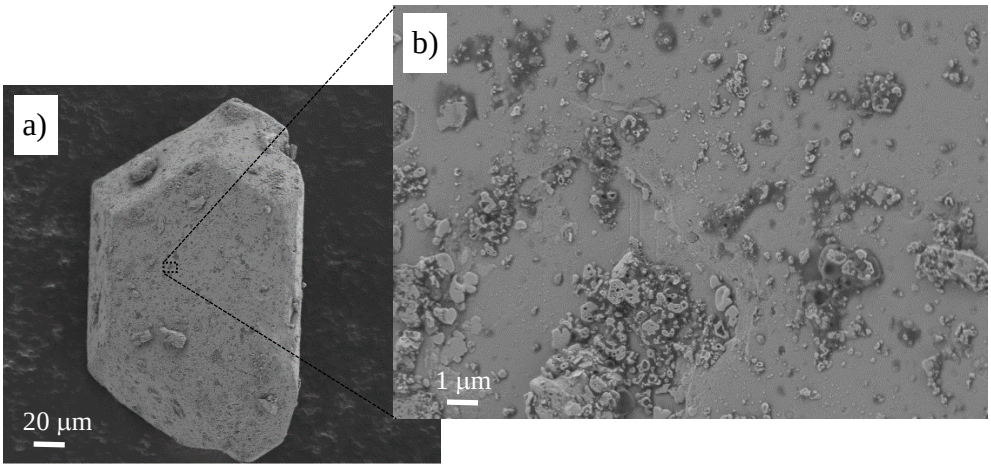

Fig. 1. SEM image of MABiI at room temperature: a) ×1000 magnification and b) ×20,000 magnification.

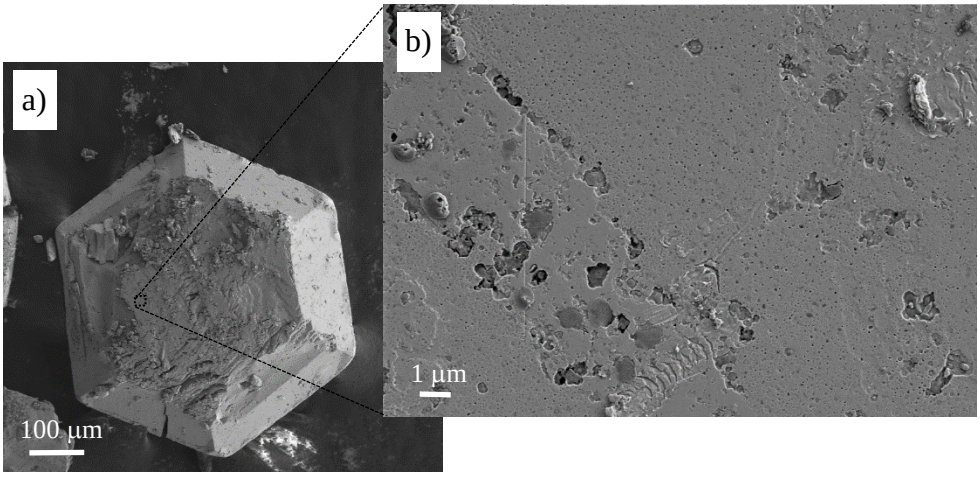

Fig. 2. SEM image of FABiI at room temperature: a) ×350 magnification and b) ×20,000 magnification.

3.1. Crystal Structure

The powder diffraction patterns of the room temperature phases of both MABiI and FABiI were indexed in the hexagonal space group, $P6_3/mmc$ and $P6_3mc$, respectively. The room temperature phase crystal structures were refined based on the models proposed by Eckhardt *et al*. [24] and Szklarz *et al.* [19] for MABiI and FABiI, respectively. The Rietveld plots for the room temperature phase of the investigated compounds are shown in Fig. 3. The refined structural parameters are presented in Table 2 and 3. Based on the structural data, the interatomic distances and angles were calculated and are given in Tables 4 and 5. The obtained structural parameters for the synthesized compounds are close to the literature values [19,24].

The XRPD studies on MABiI, confirmed that at room temperature, there are isolated bioctahedral $Bi_2I_9^{3-}$ anions in the crystal structure (Fig. 4). The two octahedra share a face and the $CH_3NH_3^+$ cations are placed on the C_3 axis rotating freely as the temperature changes (based on the IR spectra). This makes the MABiI perovskite to be 0 dimensional. The shared octahedra have only small distortion, most probably as a result of repulsion between bismuth cations in bioctahedra (Table 4). The unit cell parameters are slightly larger compared to the published data of Eckhardt *et al.* [24], as a result of larger Bi1-I1 and Bi1-I2 interatomic distances. The larger distances also affect the BVS-sums, with calculated bismuth valence of 2.94(1).

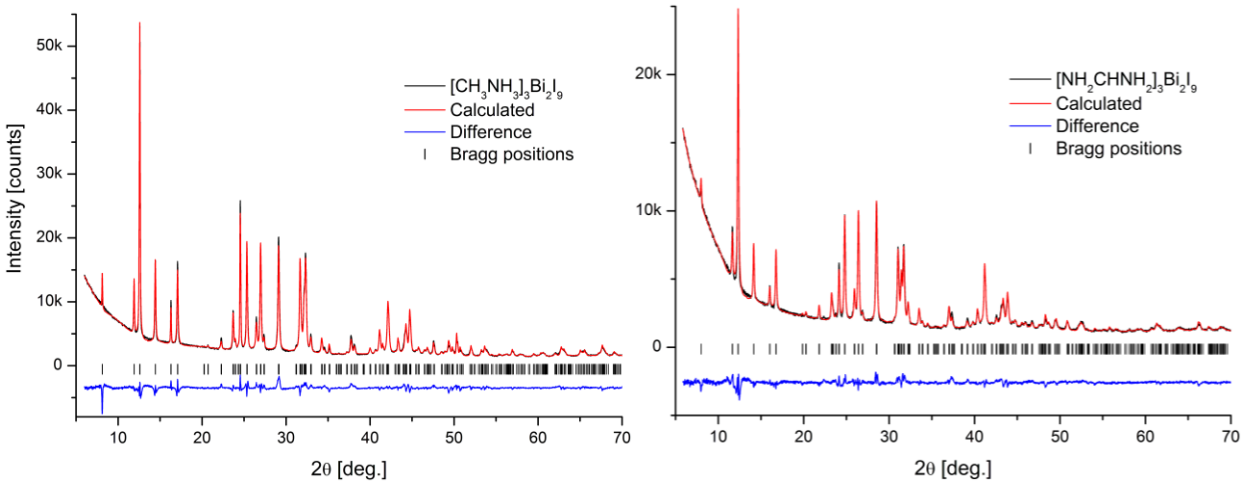

a) b)

Fig. 3. Rietveld plot of the room temperature phases of a) MABiI and b) FABiI.

Table 2. Crystal structure data of $[CH_3NH_3]_3Bi_2I_9$ at 25 °C.

Atom	**Wyck.**	***x***	***y***	***z***	**Occ.**	**Biso**
Bi1	4f	2/3	1/3	0.1541(1)	1.00	4.4(1)
I1	6h	0.4979(5)	-0.0044(1)	1/4	1.00	4.4(1)
I2	12k	0.8341(4)	0.668(1)	0.0805(1)	1.00	4.4(1)
C1*	4e	1.0000	1.0000	0.2166	0.50	4.4(1)
N1*	4e	1.0000	1.0000	0.2166	0.50	4.4(1)
N2*	4f	0.3333	-0.3333	0.0846	1.00	4.4(1)
C2*	12k	0.2300	-0.3850	0.0279	0.33	4.4(1)

* structural parameters fixed according to Eckhardt *et al.* [24]

SG. (194) $Z = 2$, $P6_3/mmc$, $a = 8.574(1)$ Å, $c = 21.746(2)$ Å,
$R_{exp} = 3.90$, $R_{wp} = 14.1$, $\chi^2 = 13.1$

Table 3. Crystal structure data of $[NH_2CHNH_2]_3Bi_2I_9$ at 25 °C.

Atom	**Wyck.**	***x***	***y***	***z***	**Occ.**	**Biso**
Bi1	2b	1/3	2/3	0.115(2)	1.00	5.3(1)
Bi2	2b	1/3	2/3	0.305(2)	1.00	5.3(1)
I1	6c	0.175(1)	0.351(1)	0.384(2)	1.00	5.3(1)
I2	6c	0.679(1)	0.840(1)	0.050(2)	1.00	5.3(1)
I3	6c	0.5013(2)	0.4987(2)	0.210(2)	1.00	5.3(1)
C1*	2a	0.0000	0.0000	0.2170	1.00	5.3(1)
N2*	12d	0.0710	0.0350	0.2710	0.333	5.3(1)
N3*	6c	–0.0830	-0.1661	0.2020	0.333	5.3(1)
C6*	2b	2/3	1/3	0.0670	1.00	5.3(1)
N7*	12d	0.6660	0.4650	0.0400	0.333	5.3(1)
C4*	2b	2/3	1/3	0.3670	1.00	5.3(1)
N5*	12d	0.6790	0.1960	0.3820	0.333	5.3(1)

* structural parameters fixed according to Szklarz *et al*. [19]

SG. (186) $Z = 2$, $P6_3mc$, $a = 8.7641(1)$ Å, $c = 22.1173(5)$ Å,
$R_{exp} = 6.48$, $R_{wp} = 14.5$, $\chi^2 = 4.98$.

Table 4. Selected interatomic distances, angles, bond-valence sums, and octahedral distortion for $[CH_3NH_3]_3Bi_2I_9$.

Bond length distances		BiI_6 polyhedra angles	
Bi1–I1/Å	3.265(3) ×3	I1-Bi1-I1/°	83.5(1) ×3
Bi1–I2/Å	2.962(3) ×3	I2-Bi1-I2/°	93.6(2) ×3
Bi1 BVS	2.94(1)	I1-Bi1-I2/°	172.9(2) ×3
$\Delta(Bi1I_6)$	$23.651 \cdot 10^{-4}$		

Table 5. Selected interatomic distances, angles, bond-valence sums, and octahedral distortion for $[NH_2CHNH_2]_3Bi_2I_9$.

Bond length distances		BiI_6 polyhedra angles	
Bi1–I2/Å	2.99(3) ×3	I1Bi2-I3/°	176.6(2) ×3
Bi1–I3/Å	3.30(4) ×3	I3-Bi2-I1/°	93.6(2) ×2
Bi2–I1/Å	2.97(4) ×3	I1-Bi2-I1/°	88.8(1) ×2

Bi2–I3/Å	3.30(4) ×3	I3-Bi2-I3/°	83.9(1) ×2
Bi1–Bi2/Å	4.20 (7)	I2-Bi1-I3/°	169.2(2) ×3
C1–N3/Å	1.303	I3-Bi1-I3/°	83.9(1) ×2
C1–N2/Å	1.310	I3-Bi1-I2/°	88.1(8) ×2
C6–N7/Å	1.302	I2-Bi1-I2/°	98.9(1) ×2
C4–N5/Å	1.304		
Bi1 BVS	2.7(1)		
$\Delta(Bi1I_6)$	$24.055 \cdot 10^{-4}$		
Bi2 BVS	2.8(1)		
$\Delta(Bi2I_6)$	$29.054 \cdot 10^{-4}$		

The crystal structure of the powder FABiI sample was solved in the $P6_3mc$ space group. According to the structure refinement and the results presented in Table 3 and 5, it is found that the position of the bioctahedral $Bi_2I_9^{3-}$ anions are very close to those in the MABiI crystal structure (Fig. 4). Again, the BiI_6 octahedra share a face, and the FA^+ cations are distributed around the isolated face shared octahedra and are connected to the iodide ion through hydrogen bonds. Compared to the MABiI, the entire lattice of FABiI is expanded due to the larger size of the FA^+ cation, and the octahedra are more distorted. Again the unit cell parameters of our sample are slightly larger, than those published by Szklarz *et al*. [19].

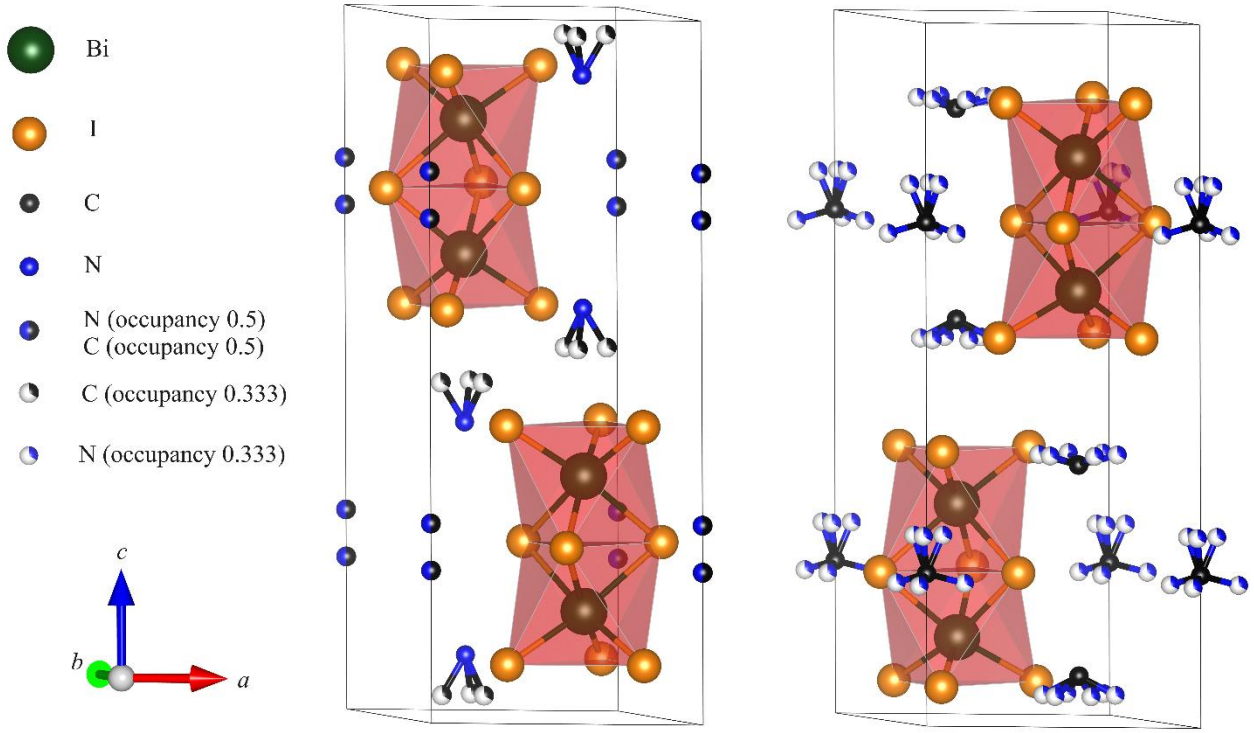

Fig. 4. Polyhedral representation of the crystal structure of MABiI (left) and FABiI (right).

3.2. IR spectroscopy and thermal analysis

In order to gain a better understanding of the structural changes that occur in these perovskites as the temperature varies, a detailed investigation using thermal analysis techniques (TG/DTA and DSC) and IR spectroscopy over a wide temperature range was conducted. The temperature range in which the studied compounds are stable was estimated by TG/DTA analysis. According to the obtained TG/DTA curves given in Fig. S1, the MABiI perovskite seems to be stable up to about 277 ºC, while FABiI is stable up to 264 ºC. Above these temperatures, the overall mass loss exceeds 1.5 %, indicating the onset of the compound's decomposition.

The analysis of the IR spectra of MABiI shows that in the low-temperature region, the compound manifests one phase transition at –128 ºC that is found to be a first-order transition. Using the appearance of the temperature-dependent isosbestic point (Fig. 5), it is possible to determine the temperature of the PT [31]. In the case of MABiI, the appearance of the isosbestic point (IP) is associated with the symmetrical stretching vibrations of the ammonium cations present in the perovskite structure. By increasing the temperature, one of the $\nu_s(NH_3^+)$ bands diminishes (at 3159 cm^{-1}), while the band at 3169 cm^{-1}, assigned as an inactive one, appears. At the same time, these bands involved in the formation of the IP are accompanied by a band shift. These changes are a strong indication of the occurrence of phase transition, a result that is confirmed by the DSC analysis performed on MABiI (discussed below in this section).

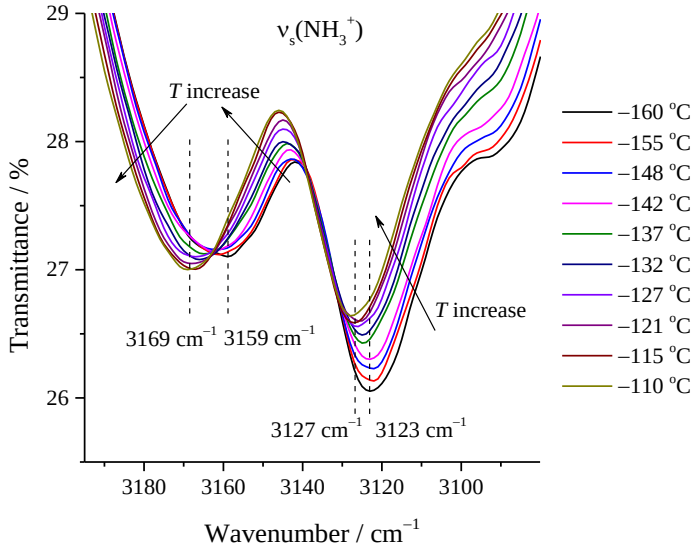

Fig. 5. First-order phase transition in the low-temperature region of MABiI detected by the appearance of isosbestic point (IP) which is used to determine the temperature of the phase transition.

The shifting of other bands, not associated with the formation of an isosbestic point, can also be used in the determination of the temperature of the phase transition, as previously established [31,32]. One of the most pronounced band shifts is observed for the symmetric stretching of NH_3^+ groups at 3123 cm^{-1} (Fig. 5) which at the same time is a neighboring band to the one forming the IP. Additional band shifts are observed for the $\delta_s(NH_3^+)$ and ν(C–N) bands, shown in Fig. S2 and Fig. S3. The analysis of these changes can be used to verify the temperature at which the change takes place. The calculated temperature for the PT based on the band shifts is in line with the temperature determined by the formation of the isosbestic point.

Using the isosbestic point, the temperature of the transition can be calculated and, in this case, we obtained a value of –128.2 ºC. Calculations based on the shifting of the neighboring band (at 3123 cm^{-1}) led to a value of –127.5 ºC. Similar results are obtained regarding the other two shifts (discussed in Supplementary material). Since the accuracy of the temperature reading is ±0.5 ºC, the PT can be estimated to be –128 ºC. The obtained value is in accordance with the literature data reported for this compound, i.e. –131 ºC by Jakubas *et al*. [23], –128 ºC by Bator *et al*. [33], and –130 ºC by Kamminga *et a*l. [25]. Our DSC measurements (Fig. 6a) comply with both the results obtained by the IR spectra and the literature data. It is interesting to note that this transition is the most intense one in the DSC curve, indicating a high-energy transition accompanied by a change in the crystal system [25], as presented in Table 6.

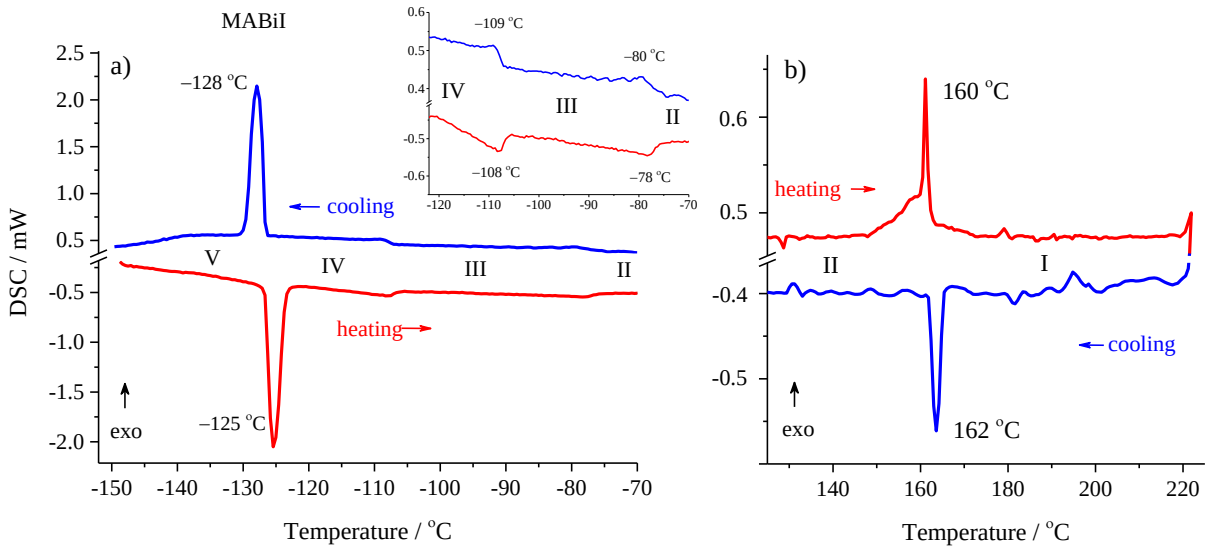

Fig. 6. DSC curve of MABiI in the temperature range from a) –150 ºC to –70 ºC and b) 130 to 220 ºC, indicating the different phases marked I to V. Inset a): up-scaled graph showing the low energy transitions in the low-temperature interval.

As reported by Bator *et al*. [33], continuous phase transitions take place at –108 ºC and –55 ºC. On the other hand, the measurements done by DSC in this study indicate phase transitions at –108 and –78 ºC upon heating the sample (–109 ºC and –80 ºC upon cooling) as presented in the

inset of Fig. 6a. Our measurements (IR and DSC) did not show any changes in the vicinity of –55 ºC (Fig. S4). Detailed analysis of the spectra in this temperature region (Fig. 7 and Fig. S5), leads to a conclusion that the transitions are continuous in the entire temperature region starting from –104.8 ºC and ending at –57.6 ºC. Based on the differences in the spectra of these starting and ending points, it can be concluded that there are two phase transitions [32,33] associated with the changes in the temperature interval in question. Further comparing the spectra given in Fig. 7 (and Fig. S5), it becomes obvious that the spectra recorded below –120 ºC resemble the ones recorded above –55 ºC. This means that the appearance of the new phase is triggered by a continuous transformation within the temperature range so the starting and ending IR spectra correspond to each other. The phase change described for MABiI has its "peak" at –78 ºC, meaning that the spectrum recorded at –78 ºC has the highest discrepancy from the spectra at –104 ºC and –58 ºC that resemble each other and are indistinguishable. Most probably, this is the point where the transition from monoclinic to hexagonal crystal structure happens, as described later. What is interesting to note is that the temperature of the maximal discrepancy found in the recorded IR spectra corresponds to a small intensity peak at the same temperature in the DSC curve (inset in Fig. 6a) accompanied by a small change in entropy presented in Table 6.

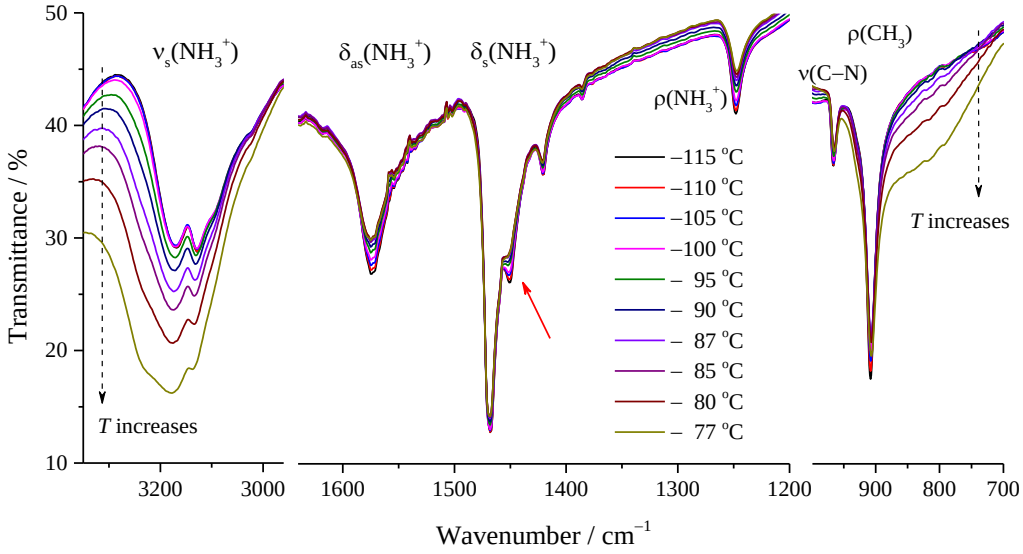

Fig. 7. Temperature-dependent IR spectra of MABiI representing the temperature point where the continuous phase transition begins and where it reaches its maximal discrepancy from the starting position.

Table 6. Changes in the enthalpy and molar entropy for the corresponding phase transitions at indicated temperatures in MABiI, upon cooling and heating.

Transition / upon cooling	Temperature / ºC	ΔH / J g^{-1}	ΔS_m / J K^{-1} mol^{-1}
I → II	+160	0.029	0.423
II → III	–80	0.048	0.431

III → IV	–109	0.046	0.471
IV → V	–128	1.680	19.60
Transition / upon heating			
V → IV	–125	–1.701	–19.60
IV → III	–108	–0.044	–0.450
III → II	–78	–0.047	–0.412
II → I	+162	–0.028	–0.409

Taking into consideration that these transitions are continuous, sometimes it is difficult to precisely determine the temperatures at which they start and end, especially by the approach used in [34]. The continuous phase transition has not been recorded by Kamminga *et al*., since they have collected the XRD patterns slightly above (–113 ºC) and below (–173 ºC) the registered PT (–130 ºC). Since they rely on the results from Jakubas *et al*. [23], they only mention two phase transitions (at –130 and –50 ºC) and they have measured the XRD patterns at temperatures corresponding to these phases (XRD at –173, –113, and +27 ºC) missing the entire temperature range where the continuous phase transition takes place.

A complete scheme of the determined phases and PTs for MABiI by this work according to IR measurement and DSC data including notation recommended by IUCr [35] will be given later. Literature data on PT in MABiI is summarized in the Supplementary material (Scheme S1).

Further inspection of the IR spectra in the temperature range from –60 to +160 ºC shows no significant changes in the spectra appearance and no phase transitions are detected. The next phase transition can be derived from the changes occurring at +160 ºC. At this point, the bands originating from the presence of CH_3 groups (3000 - 2800 cm^{-1}) reappear, and as the temperature rises, they gain intensity (Fig. S6). Since this change is not accompanied by a change in the crystal system nor the space group, it can be characterized as a continuous isostructural phase transition. The nature of this change can be due to the restrained rotation of the CH_3 groups. At higher temperatures, the CH_3 groups can rotate more freely resulting in lower sight-symmetry of the position of the CH_3 groups. This leads to the appearance of bands that are due to the ν_s vibrations and combinations. As the temperature increases the number of rotated CH_3 groups increases and this leads to higher band intensity. This finding is also confirmed by the results from the DSC measurements (Fig. 6b). The low energy change (Table 6) for the transition I → II points to a small change in the structure of the perovskite.

Summarizing the results obtained by the IR spectra of MABiI, the DSC measurements, the literature data, and the discussion given above, the following notation of the different phases have been derived based on the recommendations given by IUCr [35]:

I │ 433 - 550 K │ $P6_3/mmc$ (194) │ $Z = 2$ │ - │ decomposition above 550 K

II │ 215 - 433 K │ $P6_3/mmc$ (194) │ $Z = 2$ │ - │ -
III │ 165 - 215 K │ - │ - │- │ continuous transition from monoclinic to hexagonal at 195 K
IV │ 145 - 165 K │ $C2/c1$ (15) │ $Z = 4$ │ - │ -
V │ < 145 K │ $P2_1$ (14) │ $Z = 4$ │ - │ -

From the data given in Scheme S1 in the Supplementary material, an updated scheme (Scheme 1) is given including the findings in this work that are based on the temperature-dependent IR spectra as well as on the DSC measurements.

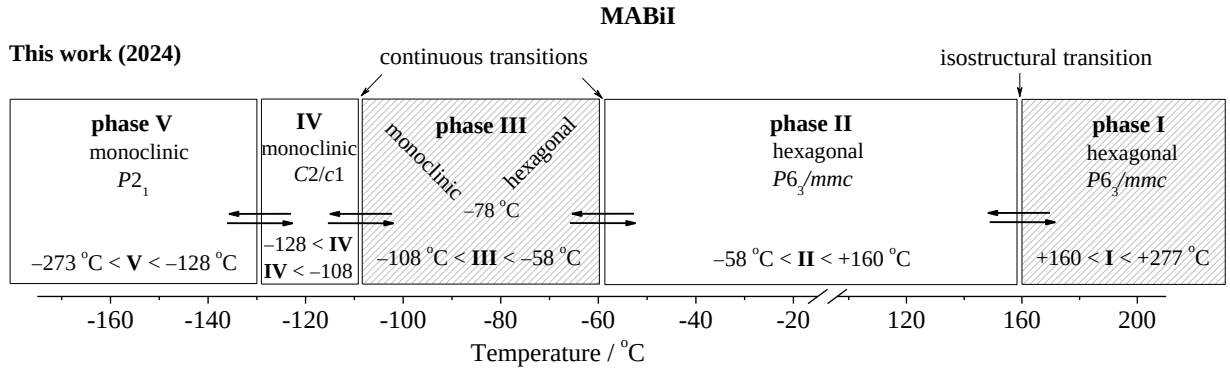

Scheme 1. Representation of the phases of MABiI and the PTs for the corresponding temperature changes.

Although the formamidinium cation is bigger than methylammonium, MABiI and FABiI are isostructural. Phase transitions of these two perovskites also show some similarities. FABiI shows one discontinuous phase transition in the low-temperature region and a continuous transition in almost the same temperature region as MABiI. Recently, results concerning the thermal behavior below room temperature have been published [19]. Our IR and DSC measurements correspond to the published data, except for one phase transition in the low-temperature region detected by DSC analysis provided by Szklarz *et al*. [19]. Namely, according to the authors, a phase transition at –153 ºC can be detected. Out of the three PTs found in the low-temperature region, this phase transition is the most pronounced one (13.2 J mol^{-1} K^{-1}). In our IR data, there are no visible changes in this temperature region, although the lower energy transitions are usually detectable by IR. The reason for the appearance of the peak at –153 ºC in the DSC curve examined by Szklarz *et al* might be due to the inclusion of water molecules in the crystals. The synthesis conducted in the mentioned study [19] is performed in HI and the recrystallization is done from water. This leaves a high probability of water molecules being incorporated into the system. It is reported that the phase transition of ice XV → VI at atmospheric pressure starts at –153 ºC and most of the ice XV disorders near –142 ºC taking up the heat. These temperatures precisely correspond to the ones reported in [19]. There is a possibility that the signal in the DSC curves [19] arises from the presence of ice [36,37]. This can also be confirmed by the sudden weakening of the dielectric response when ice VI

transforms to ice XV upon cooling, reported by [38] and visible in the work of Szklarz *et al*. Based on these findings one could conclude that the phase transition registered at –153 ºC probably originates from the water present in FABiI crystals.

On the other hand, the phase transition at –138.5 ºC noted by Szklarz *et al*. can also be identified using IR spectroscopy (Fig. 8) and DSC even though its ΔS value is low (1.3 [19] and 1.1 J mol^{-1} K^{-1} [this work]). These changes in the IR spectra are observable in the region 1050 to 1037 cm^{-1} (Fig. 8b). The band at 1047 cm^{-1} starts to gain intensity triggered by the phase transition at –143 ºC, while the band at 1041 cm^{-1} vanishes when the transition at –136 ºC is completed. The temperature of the phase transition detected by the employed IR method (–136.8°C) is slightly different, but still very close to the one obtained by the DSC analysis (–138.0 ºC, Fig. 9).

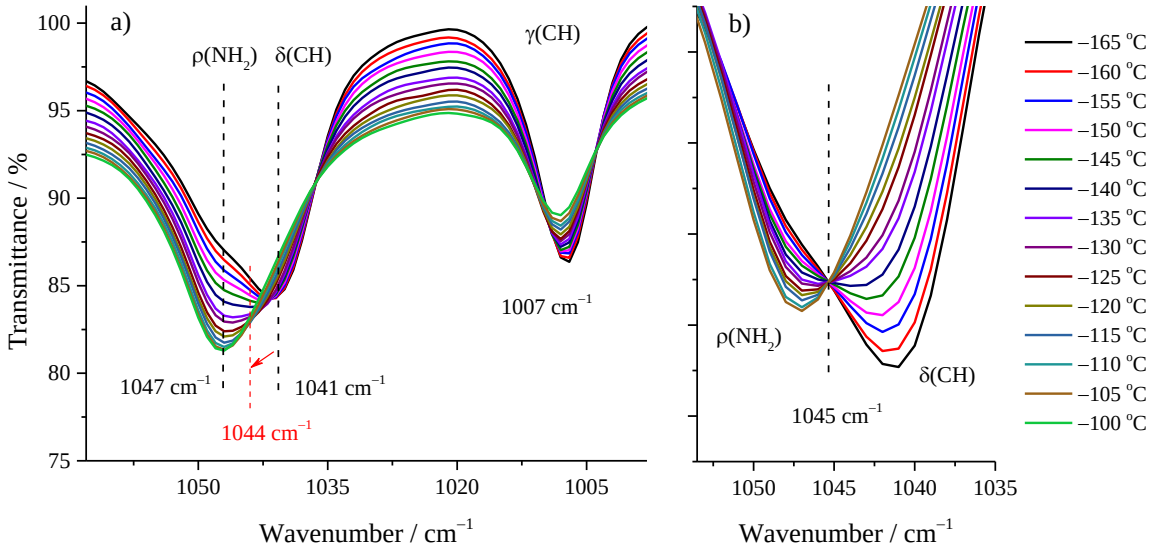

Fig. 8. Spectral region used to determine the temperature of the PT in FABiI, a) raw IR data clearly showing the band shift of the banding CH vibrations, b) isosbestic point obtained after the normalization where the vanishing and the appearance of the bands constituting the IP is visible.

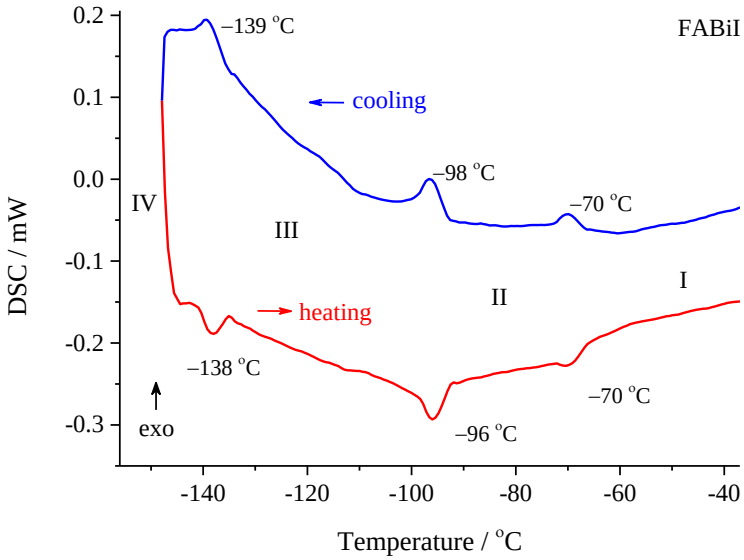

Fig. 9. DSC curve of FABiI in the temperature range from –150 ºC to –40 ºC, indicating the different phases marked I to IV.

This PT is accompanied by the appearance of an isosbestic point (Fig. 8). Even when the raw data (not normalized) are considered (Fig. 8a), the presence of an IP is distinguishable. The bands representing the banding CH vibrations do not only shift from 1041 cm^{-1} (–165 ºC) to 1044 cm^{-1} (–120 ºC, last observed) but at the same time diminish, while the bands originating from the rocking NH_2 vibration (1044 cm^{-1}) appear. If the spectra are normalized [39], the IP is observed at 1045 cm^{-1} (Fig. 8b). Through calculation, it has been determined that the temperature at which the phase transition occurs is –136.8°C. The band from the out-of-plane bending CH vibrations can also be used to calculate the phase transition temperature. This band appears at 1007 cm^{-1} for the spectra recorded below –150 ºC and shifts as the temperature increases. The calculated PT temperature using this band is found to be –137.2 ºC.

The similarities between FABiI and MABiI are especially noticeable in the temperature region above –100 ºC where the continuous phase transition takes place. In the case of FABiI, the transition starts at –96.5 ºC (Fig. 10) and ends at –50.6 ºC (Fig. S7) reaching its maximum divergence from the initial state at –70 ºC. This increasing intensity of the bands in the region of stretching vibrations during the phase transition and the fact that they become broader can be an implication of the appearance (or increase) of hydrogen bonding in the system. Additionally, the band at 825 cm^{-1}, assigned as a combinational band, γ(NH) + γ(CH) becomes IR active [40]. This band has been assigned only for the free formamidine molecules, while in the compounds containing the formamidinium ion, its presence has not been detected [40–42]. In this region, the inactive wagging vibration of the NCN should also become active. This band does not appear in the IR spectra of FA^+ compounds recorded at room temperature [43,44]. Analyzing the complex

band at 825 cm^{-1} it is obvious that not only the combinational band γ(NH) + γ(CH) is present (with a maximum at 838 cm^{-1}) but also a band at 811 cm^{-1}, that can be assigned as the waging NCN vibration. The evolution of these two bands is especially noticeable for the spectra recorded at –70 ºC and above (Fig. 10).

The correct assignation of this band can be confirmed by the comparison of the spectra of the continuous phase transition for MA and FABiI. The band at 825 cm^{-1} is not present and does not appear in MABiI spectra since there are no CN_2 or CN_3 fragments to perform this kind of wagging vibration. Moreover, in the detailed analysis of the IR spectra of $GUAPbI_3$ [32,45,46], the appearance of the band at 821 cm^{-1} is assigned to the wagging CN_3 vibrations, this provides additional validation of the assignation of the discussed band. On the other hand, the broadening of the band at 825 cm^{-1}, not only points out its combinational nature but also points to the fact that the groups associated with the appearance of the band are at the same time involved in hydrogen bonding. This conclusion is reasonable since the main contribution to the combinational band is by γ(NH), i.e. 73 % [40].

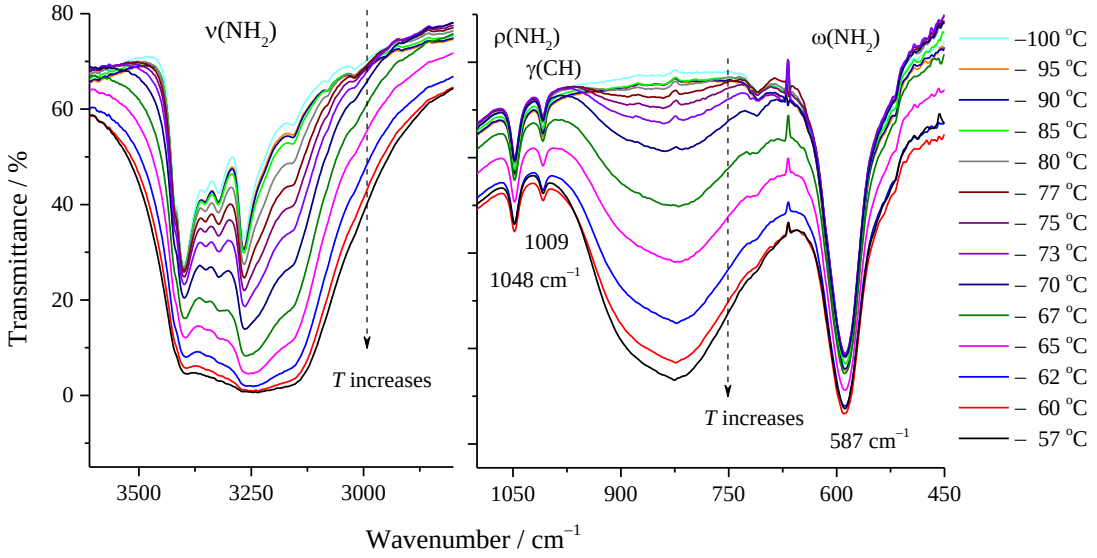

Fig. 10. Continuous phase transition in FABiI in the temperature range from –100 ºC to –57 ºC where the maximal deviation from the "pre-transition" state occurs. The arrows indicate the evolution of the spectra as the temperature increases.

Flipping of the FA^+ cation in FABiI may be the trigger of the continuous phase transition and changes in the IR spectra, similar to the changes of the GUA^+ cation in $GUAPbI_3$ [32]. The strongest indication for this structural change is the appearance and diminishing of the band at 825 cm^{-1}. Specifically, the intensity of this band gradually increases reaching its maximum when the rotation (flipping) around the C_2 axis of the FA^+ is 90 º. Then the profile of the band goes

back to its previous position as the rotation reaches 180 º or as the “in-plane” flipping is complete.

The changes occurring in the IR spectra in this temperature region are confirmed by the DSC analysis (Fig. 9), as well. The low-intensity signals indicate low energy transitions (Table 7), accompanied by small changes in the enthalpy of the transition. These kinds of changes are only possible when a PT is not accompanied by a change in the crystal system or the space group.

Table 7. Changes in the enthalpy and molar entropy for the corresponding phase transition at the indicated temperatures in FABiI, upon cooling and heating.

Transition / upon cooling	Temperature / ºC	ΔH / J g^{-1}	ΔS_m / J K^{-1} mol^{-1}
I → II	–70	0.052	0.433
II → III	–98	0.111	1.079
III → IV	–139	0.034	0.506
Transition / upon heating			
IV → III	–138	–0.040	–0.508
III → II	–96	–0.115	–1.102
II → I	–70	–0.052	–0.431

According to the findings based on the temperature-dependent IR analysis and the TG/DTA, it can be concluded that in FABiI, there is one discontinuous PT of first order and one continuous transition in the temperature region from –170 to +200 ºC. These results are summarized in Scheme 2, followed by a systematic depiction with notation recommended by the IUCr.

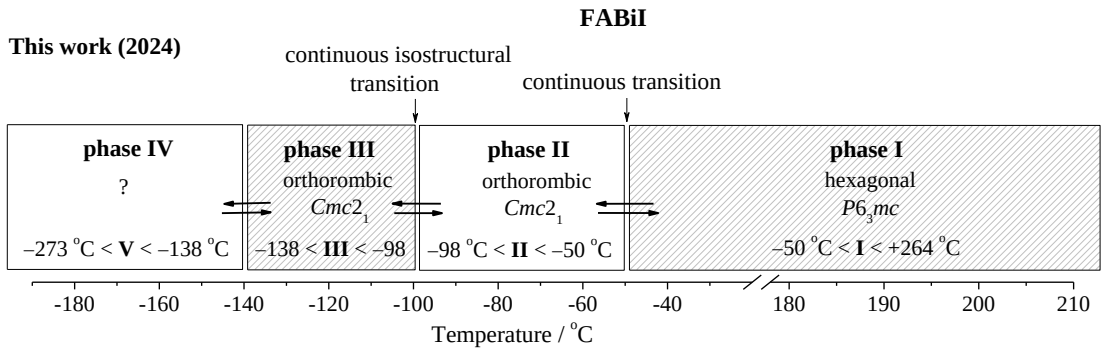

Scheme 2. Schematic representation of the phases of FABiI and the corresponding PTs found by this work for the corresponding temperature changes.

I | 223 - 537 K | $P6_3mc$ (186) | Z = 2 | - | decomposition above 537 K
II | 175 - 223 K | $Cmc2_1$ (36) | Z = 4 | - | -
III | 156 - 175 K | $Cmc2_1$ (36) | Z = 4 | - | -

IV | < 156 K | - | - | - | -

Based on the results obtained by the DSC, the most energetic change during PT in the structure of MABiI is associated with the reorientation of the NH_3^+ groups (19.60 J K^{-1} mol^{-1}). In the case of FABiI detected energy changes are considerably smaller compared to the aforementioned change in MABiI. This can be ascribed to the geometry, nature, and position of the MA^+ and FA^+ cations in the crystal structure. Even though MA^+ is smaller in size it is less prone to movement (i.e. its parts CH_3 and NH_3) compared to FA^+ (the two NH_2 groups and the N–C–N delocalized electrons). The movement along the C_2 axis in FA^+ is more energetically favorable than the movement along the C–N bond in MA^+ especially when we add to this consideration the pronounced hydrogen bond present in these perovskites.

4. Conclusion

Well-shaped microcrystals of formamidinium bismuth iodide, $[(CH(NH_2)_2]_3Bi_2I_9$, FABiI and methylammonium bismuth iodide, $[CH_3NH_3]_3Bi_2I_9$, MABiI were prepared and analyzed using different techniques for structure characterization (X-ray powder diffraction and IR spectroscopy) as well as thermal characterization (TG/DTA, DSC, temperature-dependent IR spectroscopy). According to the results obtained by XRPD, the crystal structure of MABiI and FABiI was refined, and it was determined that both compounds crystalize in the centrosymmetric hexagonal groups $P6_3/mmc$ and $P6_3mc$, respectively. Their crystal structure consists of bioctahedral $Bi_2I_9^{3-}$ anions surrounded by MA^+ or FA^+ cations that are attracted by the hydrogen atoms to the iodides from the BiI_6 octahedra via hydrogen bonding. In both compounds, the octahedra are distorted and two octahedra share a face. These so-defined bioctahedra are isolated making the MA and FABiI zero-dimensional perovskites.

By analyzing the temperature-dependent IR spectra combined with DSC measurements it was found that there are some inconsistencies with the previously reported PTs. The results reveal one first-order transition at –128 ºC, two continuous PT at –105 and –58 ºC, and one isostructural PT at +160 ºC for MABiI. Concerning the PTs in FABiI, it is evident that it shows one discontinuous phase transition at –138 ºC and a continuous transition in almost the same temperature region as MABiI (–98 and –50 ºC). The energy changes of the PTs point to the mobility of the MA^+ and FA^+ parts in the structure. The first-order PT in MABiI is accompanied by much higher energy change (two orders of magnitude) compared to the other detected transitions, both in MABiI and FABiI.

Acknowledgment

The authors kindly acknowledge the financial support obtained by the Ministry of Education and Science of N. Macedonia in the scope of the project for “Support for development of laboratory

resources" 08-15590/2 (Modernization and development of the laboratory for structure characterization of materials), the Ministry of Higher Education, Science and Innovation of the Republic of Slovenia through grants P1-0175 (Advanced Inorganic Chemistry) and The Centre for Research Infrastructure at the Faculty of Chemistry and Chemical Technology (IC UL FCCT).

5. References

[1] A. Kojima, K. Teshima, Y. Shirai, T. Miyasaka, Organometal Halide Perovskites as Visible-Light Sensitizers for Photovoltaic Cells, J. Am. Chem. Soc. 131 (2009) 6050–6051. https://doi.org/10.1021/ja809598r.

[2] H.-S. Kim, C.-R. Lee, J.-H. Im, K.-B. Lee, T. Moehl, A. Marchioro, S.-J. Moon, R. Humphry-Baker, J.-H. Yum, J.E. Moser, M. Grätzel, N.-G. Park, Lead Iodide Perovskite Sensitized All-Solid-State Submicron Thin Film Mesoscopic Solar Cell with Efficiency Exceeding 9%, Sci. Rep. 2 (2012) 591. https://doi.org/10.1038/srep00591.

[3] National Renewable Energy Laboratory, Best Research-Cell Efficiency Chart, Natl. Renew. Energy Lab. (2022). https://www.nrel.gov/pv/assets/pdfs/best-research-cell-efficiencies-rev220630.pdf.

[4] R.J.D. Tilley, Perovskites: Structure–Property Relationships, John Wiley & Sons, Ltd, Chichester, UK, 2016. https://doi.org/10.1002/9781118935651.

[5] A.D. Jodlowski, A. Yépez, R. Luque, L. Camacho, G. de Miguel, Benign-by-Design Solventless Mechanochemical Synthesis of Three-, Two-, and One-Dimensional Hybrid Perovskites, Angew. Chemie Int. Ed. 55 (2016) 14972–14977. https://doi.org/10.1002/anie.201607397.

[6] A. D'Annibale, R. Panetta, O. Tarquini, M. Colapietro, S. Quaranta, A. Cassetta, L. Barba, G. Chita, A. Latini, Synthesis, physico-chemical characterization and structure of the elusive hydroxylammonium lead iodide perovskite NH_3OHPbI_3, Dalt. Trans. 48 (2019) 5397–5407. https://doi.org/10.1039/C9DT00690G.

[7] E. V. Campbell, B. Dick, A.L. Rheingold, C. Zhang, X. Liu, Z. V. Vardeny, J.S. Miller, Structures of a Complex Hydrazinium Lead Iodide, $(N_2H_5)_{15}Pb_3I_{21}$, Possessing $[Pb_2I_9]^{5-}$, $[PbI_6]^{4-}$, and I^- Ions and α- and β-(N2H5)PbI3, Chem. - A Eur. J. 24 (2018) 222–229. https://doi.org/10.1002/chem.201704356.

[8] C. Seth, D. Jana, V. Jindal, D. Khushalani, S. Ghosh, One-Dimensional Behavior of Imidazolium Lead Iodide, J. Phys. Chem. C. 123 (2019) 16449–16455. https://doi.org/10.1021/acs.jpcc.9b03894.

[9] A.F. Xu, R.T. Wang, W. Yang, V. Jarvis, J.F. Britten, G. Xu, Pyrrolidinium lead iodide from crystallography: A new perovskite with low bandgap and good water resistance, Chem. Commun. 55 (2019) 3251–3253. https://doi.org/10.1039/c8cc10135c.

[10] S.R. Pering, W. Deng, J.R. Troughton, P.S. Kubiak, D. Ghosh, R.G. Niemann, F. Brivio, F.E. Jeffrey, A.B. Walker, M.S. Islam, T.M. Watson, P.R. Raithby, A.L. Johnson, S.E. Lewis, P.J. Cameron, Azetidinium lead iodide for perovskite solar cells, J. Mater. Chem. A. 5 (2017) 20658–20665. https://doi.org/10.1039/C7TA07545F.

[11] F.S. Galasso, Perovskites and high Tc superconductors, Gordon and Breach Science Publishers, New York, 1990.

[12] R.K. Misra, B. Cohen, L. Iagher, L. Etgar, Low-Dimensional Organic–Inorganic Halide Perovskite: Structure, Properties, and Applications, ChemSusChem. 10 (2017) 3712–

3721. https://doi.org/10.1002/cssc.201701026.
[13] T. Lu, H. Li, M. Li, S. Wang, W. Lu, Inverse Design of Hybrid Organic–Inorganic Perovskites with Suitable Bandgaps via Proactive Searching Progress, ACS Omega. 7 (2022) 21583–21594. https://doi.org/10.1021/acsomega.2c01380.
[14] J. Marí-Guaita, A. Bouich, M.A. Shafi, A. Bouich, B. Marí, Investigation on the Stability and Efficiency of $MAPbI_3$ and $MASnI_3$ Thin Films for Solar Cells, Phys. Status Solidi. 219 (2022) 2100664. https://doi.org/10.1002/pssa.202100664.
[15] C. Lan, G. Liang, S. Zhao, H. Lan, H. Peng, D. Zhang, H. Sun, J. Luo, P. Fan, Lead-free formamidinium bismuth perovskites $(FA)_3Bi_2I_9$ with low bandgap for potential photovoltaic application, Sol. Energy. 177 (2019) 501–507. https://doi.org/10.1016/j.solener.2018.11.050.
[16] A. Khan, S. Han, X. Liu, K. Tao, D. Dey, J. Luo, Z. Sun, A new antimony-based organic–inorganic hybrid absorber with photoconductive response, Inorg. Chem. Front. 5 (2018) 3028–3032. https://doi.org/10.1039/C8QI00902C.
[17] Y. El Ajjouri, V.S. Chirvony, N. Vassilyeva, M. Sessolo, F. Palazon, H.J. Bolink, Low-dimensional non-toxic $A_3Bi_2X_9$ compounds synthesized by a dry mechanochemical route with tunable visible photoluminescence at room temperature, J. Mater. Chem. C. 7 (2019) 6236–6240. https://doi.org/10.1039/C9TC01765H.
[18] X. Zheng, W. Zhao, P. Wang, H. Tan, M.I. Saidaminov, S. Tie, L. Chen, Y. Peng, J. Long, W.-H. Zhang, Ultrasensitive and stable X-ray detection using zero-dimensional lead-free perovskites, J. Energy Chem. 49 (2020) 299–306. https://doi.org/10.1016/j.jechem.2020.02.049.
[19] P. Szklarz, A. Gągor, R. Jakubas, P. Zieliński, A. Piecha-Bisiorek, J. Cichos, M. Karbowiak, G. Bator, A. Ciżman, Lead-free hybrid ferroelectric material based on formamidine: $[NH_2CHNH_2]_3Bi_2I_9$, J. Mater. Chem. C. 7 (2019) 3003–3014. https://doi.org/10.1039/C8TC06458J.
[20] W. Li, D. Xin, S. Tie, J. Ren, S. Dong, L. Lei, X. Zheng, Y. Zhao, W.-H. Zhang, Zero-Dimensional Lead-Free $FA_3Bi_2I_9$ Single Crystals for High-Performance X-ray Detection, J. Phys. Chem. Lett. 12 (2021) 1778–1785. https://doi.org/10.1021/acs.jpclett.1c00090.
[21] Y. Yamada, M. Hoyano, R. Akashi, K. Oto, Y. Kanemitsu, Impact of Chemical Doping on Optical Responses in Bismuth-Doped $CH_3NH_3PbBr_3$ Single Crystals: Carrier Lifetime and Photon Recycling, J. Phys. Chem. Lett. 8 (2017) 5798–5803. https://doi.org/10.1021/acs.jpclett.7b02508.
[22] F. Ünlü, A. Kulkarni, K. Lê, C. Bohr, A. Bliesener, S.D. Öz, A.K. Jena, Y. Ando, T. Miyasaka, T. Kirchartz, S. Mathur, Single- or double A-site cations in $A_3Bi_2I_9$ bismuth perovskites: What is the suitable choice?, J. Mater. Res. 36 (2021) 1794–1804. https://doi.org/10.1557/s43578-021-00155-z.
[23] R. Jakubas, J. Zaleski, L. Sobczyk, Phase transitions in $(CH_3NH_3)_3Bi_2I_9$ (MAIB), Ferroelectrics. 108 (1990) 109–114. https://doi.org/10.1080/00150199008018741.
[24] K. Eckhardt, V. Bon, J. Getzschmann, J. Grothe, F.M. Wisser, S. Kaskel, Crystallographic insights into $(CH_3NH_3)_3(Bi_2I_9)$: a new lead-free hybrid organic–inorganic material as a potential absorber for photovoltaics, Chem. Commun. 52 (2016) 3058–3060. https://doi.org/10.1039/C5CC10455F.
[25] M.E. Kamminga, A. Stroppa, S. Picozzi, M. Chislov, I.A. Zvereva, J. Baas, A. Meetsma, G.R. Blake, T.T.M. Palstra, Polar Nature of $(CH_3NH_3)_3Bi_2I_9$ Perovskite-Like Hybrids, Inorg. Chem. 56 (2017) 33–41. https://doi.org/10.1021/acs.inorgchem.6b01699.

[26] S. Öz, J.-C. Hebig, E. Jung, T. Singh, A. Lepcha, S. Olthof, F. Jan, Y. Gao, R. German, P.H.M. van Loosdrecht, K. Meerholz, T. Kirchartz, S. Mathur, Zero-dimensional $(CH_3NH_3)_3Bi_2I_9$ perovskite for optoelectronic applications, Sol. Energy Mater. Sol. Cells. 158 (2016) 195–201. https://doi.org/10.1016/j.solmat.2016.01.035.
[27] R.L.Z. Hoye, R.E. Brandt, A. Osherov, V. Stevanović, S.D. Stranks, M.W.B. Wilson, H. Kim, A.J. Akey, J.D. Perkins, R.C. Kurchin, J.R. Poindexter, E.N. Wang, M.G. Bawendi, V. Bulović, T. Buonassisi, Methylammonium Bismuth Iodide as a Lead-Free, Stable Hybrid Organic–Inorganic Solar Absorber, Chem. – A Eur. J. 22 (2016) 2605–2610. https://doi.org/10.1002/chem.201505055.
[28] S.S. Shin, J.P. Correa Baena, R.C. Kurchin, A. Polizzotti, J.J. Yoo, S. Wieghold, M.G. Bawendi, T. Buonassisi, Solvent-Engineering Method to Deposit Compact Bismuth-Based Thin Films: Mechanism and Application to Photovoltaics, Chem. Mater. 30 (2018) 336–343. https://doi.org/10.1021/acs.chemmater.7b03227.
[29] M.-C. Tang, D. Barrit, R. Munir, R. Li, J.M. Barbé, D.-M. Smilgies, S. Del Gobbo, T.D. Anthopoulos, A. Amassian, Bismuth-Based Perovskite-Inspired Solar Cells: In Situ Diagnostics Reveal Similarities and Differences in the Film Formation of Bismuth- and Lead-Based Films, Sol. RRL. 3 (2019) 1800305. https://doi.org/10.1002/solr.201800305.
[30] J. Rodriguez-Carvajal, FULLPROF: A Program for Rietveld Refinement and Pattern Matching Analysis, in: Abstr. Satell. Meet. Powder Diffr. XV Congr. IUCr, Toulouse, France, 1990: p. 127.
[31] M. Bukleski, S. Dimitrovska-Lazova, V. Makrievski, S. Aleksovska, A simple approach for determination of the phase transition temperature using infrared temperature-induced isosbestic points, Spectrochim. Acta - Part A Mol. Biomol. Spectrosc. 231 (2020) 118118. https://doi.org/10.1016/j.saa.2020.118118.
[32] S. Dimitrovska-Lazova, M. Bukleski, P. Tzvetkov, M. Pecovska-Gjorgjevich, D. Kovacheva, S. Aleksovska, The mechanism of the isostructural phase transition in $C(NH_2)_3PbI_3$ as a guide for understanding the properties of the new phase, Mater. Chem. Phys. 275 (2022) 125240. https://doi.org/10.1016/j.matchemphys.2021.125240.
[33] G. Bator, R. Jakubas, J. Baran, H. Ratajczak, Infrared studies of structural phase transitions in $(CH_3NH_3)_3Bi_2I_9$ (MAIB), J. Mol. Struct. 325 (1994) 45–51. https://doi.org/10.1016/0022-2860(94)80016-2.
[34] G. Bator, J. Baran, R. Jakubas, H. Ratajczak, Infrared studies on structural phase transitions in $[NH_2(CH_3)_2]_3Sb_2Br_9$ and $[NH_2(CH_3)_2]_3Sb_2I_9$, Vib. Spectrosc. 6 (1994) 193–204. https://doi.org/10.1016/0924-2031(94)85006-2.
[35] J.C. Tolédano, A.M. Glazer, T. Hahn, E. Parthé, R.S. Roth, R.S. Berry, R. Metselaar, S.C. Abrahams, Structural phase transition nomenclature report of an IUCr working group on phase transition nomenclature, Acta Crystallogr. Sect. A Found. Crystallogr. 54 (1998) 1028–1033. https://doi.org/10.1107/S0108767398008150.
[36] T.M. Gasser, A. V. Thoeny, V. Greussing, T. Loerting, Calorimetric Investigation of Hydrogen-Atom Sublattice Transitions in the Ice VI/XV/XIX Trio, J. Phys. Chem. B. 125 (2021) 11777–11783. https://doi.org/10.1021/acs.jpcb.1c07508.
[37] C.G. Salzmann, P.G. Radaelli, E. Mayer, J.L. Finney, Ice XV: A New Thermodynamically Stable Phase of Ice, Phys. Rev. Lett. 103 (2009) 105701. https://doi.org/10.1103/PhysRevLett.103.105701.
[38] R. Yamane, K. Komatsu, J. Gouchi, Y. Uwatoko, S. Machida, T. Hattori, H. Ito, H. Kagi, Experimental evidence for the existence of a second partially-ordered phase of ice VI,

Nat. Commun. 12 (2021) 1129. https://doi.org/10.1038/s41467-021-21351-9.
[39] M. Bukleski, V. Ivanovski, E. Hey-Hawkins, A direct method of quantification of maximal chemisorption of 3-aminopropylsilyl groups on silica gel using DRIFT spectroscopy, Spectrochim. Acta - Part A Mol. Biomol. Spectrosc. 149 (2015). https://doi.org/10.1016/j.saa.2015.04.026.
[40] E. Kucharska, J. Hanuza, A. Ciupa, M. Mączka, L. Macalik, Vibrational properties and DFT calculations of formamidine-templated Co and Fe formates, Vib. Spectrosc. 75 (2014) 45–50. https://doi.org/10.1016/j.vibspec.2014.09.001.
[41] A.J. Harding, K.D. Dobson, B.A. Ogunnaike, W.N. Shafarman, Thermal and Structural Characterization of Methylammonium- and Formamidinium-Halide Salts, Phys. Status Solidi. 218 (2021) 2100246. https://doi.org/10.1002/pssa.202100246.
[42] D.B. Mitzi, K. Liang, Synthesis, Resistivity, and Thermal Properties of the Cubic Perovskite $NH_2CH{=}NH_2SnI_3$ and Related Systems, J. Solid State Chem. 134 (1997) 376–381. https://doi.org/10.1006/jssc.1997.7593.
[43] M. Bukleski, S. Dimitrovska-Lazova, S. Aleksovska, Vibrational spectra of methylammonium iodide and formamidinium iodide in a wide temperature range, Maced. J. Chem. Chem. Eng. 38 (2019) 237–252. https://doi.org/10.20450/mjcce.2019.1940.
[44] M. Kuhn, R. Mecke, IR-Spektroskopische Strukturuntersuchungen über Addukte aus Cyanamid und Halogenwasserstoff, Chem. Ber. 94 (1961) 3016–3022. https://doi.org/10.1002/cber.19610941129.
[45] S. Dimitrovska-Lazova, M. Bukleski, P. Tzvetkov, S. Aleksovska, D. Kovacheva, Crystal structure of the high-temperature polymorph of $C(NH_2)_3PbI_3$ and its thermal decomposition, J. Alloys Compd. 864 (2021) 158104. https://doi.org/10.1016/j.jallcom.2020.158104.
[46] M. Bukleski, S. Dimitrovska-Lazova, S. Aleksovska, Temperature dependent phase transitions and their relation to isosbestic point formation. Case study of $C(NH_2)_3PbI_3$, Spectrochim. Acta Part A Mol. Biomol. Spectrosc. 266 (2022) 120462. https://doi.org/10.1016/j.saa.2021.120462.